iScience

Article

Phosphorylated Y14 condensates as a scaffold for DNA double-strand break repair

Graphical abstract

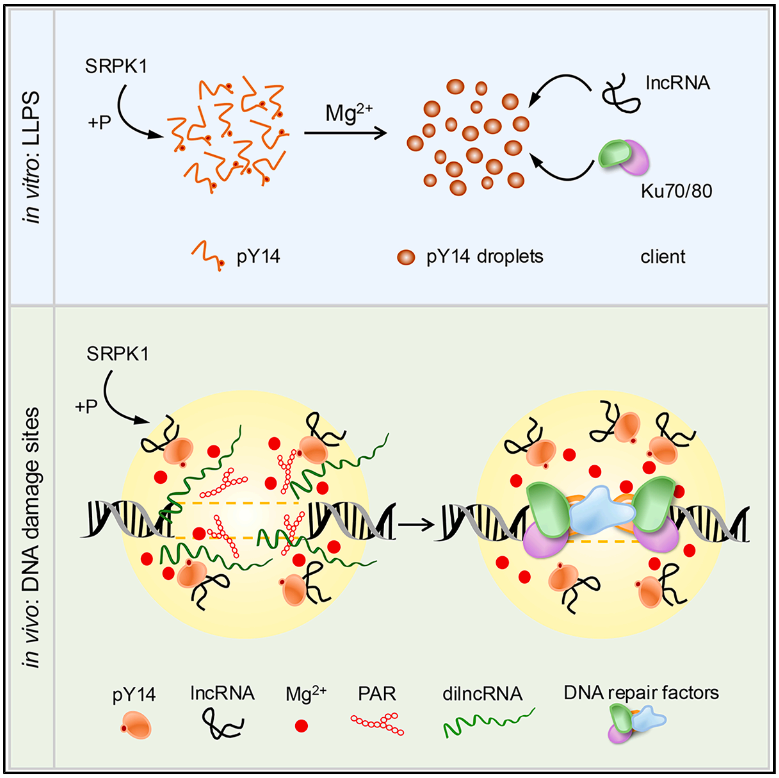

Authors

Chun-Hao Su, Tzu-Wei Chuang,
Hsin-Hong Yeh, Chiu-Lun Shen,
Pei-Yu Hung, Ying Li, Woan-Yuh Tarn

Correspondence

wtarn@ibms.sinica.edu.tw

In brief

Biochemistry; Molecular biology

Highlights

- Y14 forms condensates at DNA damage sites in a phosphorylation-dependent manner
- Phase separation of phosphorylated Y14 *in vitro* requires Mg^{2+}
- Cell-permeable EDTA disrupts Y14 condensates and repair factor recruitment at DSBs
- Disruption of Y14 condensates can improve the efficacy of anticancer agents

Su et al., 2025, iScience *28*, 113073
August 15, 2025
https://doi.org/10.1016/j.isci.2025.113073

iScience

CellPress
OPEN ACCESS

Article

Phosphorylated Y14 condensates as a scaffold for DNA double-strand break repair

Chun-Hao Su,[1,4] Tzu-Wei Chuang,[1,4] Hsin-Hong Yeh,[1,4] Chiu-Lun Shen,[1] Pei-Yu Hung,[1,2] Ying Li,[3] and Woan-Yuh Tarn[1,5,*]
[1]Institute of Biomedical Sciences, Academia Sinica, Taipei 11529, Taiwan
[2]Institute of Molecular Medicine, College of Medicine, National Taiwan University, Taipei 100233, Taiwan
[3]Department of Chemistry, University of Hong Kong, Hong Kong 999077, China
[4]These authors contributed equally
[5]Lead contact
*Correspondence: wtarn@ibms.sinica.edu.tw
https://doi.org/10.1016/j.isci.2025.113073

SUMMARY

Various DNA damage response factors form biomolecular condensates at DNA lesions. Targeting phase separation in DNA repair factor assemblies may provide a potential anticancer strategy. An RNA-binding protein, Y14/RBM8A, facilitates the repair of DNA double-strand breaks (DSBs) via its RNA-mediated interaction with non-homologous end joining (NHEJ) factors. HaloTag-Y14 fusion is distributed to laser-induced DNA damage sites in an RNA-dependent manner. Serine/arginine (SR) protein kinase 1-mediated phosphorylation of Y14 was also crucial for its localization at DNA lesions and function in DSB repair. Magnesium promoted liquid-liquid phase separation of phosphorylated Y14 *in vitro*. Ku70/80 could partition into phosphorylated Y14 condensates. Chelation of divalent cations abolished Y14 localization and subsequent recruitment of NHEJ factors at DNA damage sites. Inhibition of Y14 phosphorylation interfered with Ku70/80 recruitment and increased the sensitivity of cancer cells to DNA damage. This study reinforces that manipulating DNA repair foci can improve the efficacy of anticancer agents.

INTRODUCTION

A variety of intracellular and extracellular insults continuously cause DNA damage. To maintain genomic stability and cell homeostasis, DNA lesions must be repaired effectively. DNA double-strand breaks (DSBs) are one of the most harmful genomic lesions.[1,2] DSBs result from genotoxic agents or transcription and replication blockades and are principally repaired by two major pathways, i.e., non-homologous end joining (NHEJ) and homologous recombination (HR). HR occurs during the S/G2 phases of the cell cycle, using homologous DNA as a template, and also operates in transcriptionally active regions.[3] NHEJ occurs at a higher frequency than HR and functions throughout all stages of the cell cycle. In the NHEJ pathway, the Ku70/80 heterodimer recognizes DSB sites and stimulates the activity of DNA-dependent protein kinase catalytic subunit (DNA-PKcs).[1] Subsequently, NHEJ factors, including X-ray repair cross complementing 4 (XRCC4), XRCC4-like factor (XLF), DNA ligase IV (LIG4), endonuclease Artemis, and additional enzymes, are recruited for DNA end processing, if required, and ligation.[1]

In response to DSB, DNA damage response (DDR) signaling determines the repair pathways and elicits cellular responses such as activation of cell cycle checkpoints and/or initiation of cell apoptosis.[4] DDR involves phosphatidylinositol-3-kinase-like kinases (such as DNA-PK, ATM, and ATR), poly(ADP-ribose) polymerase 1 (PARP1), and various ubiquitination enzymes. DDR kinases coordinate a network of signaling cascades for DNA repair.[4,5] PARP1 catalyzes poly(ADP-ribosylation) (PAR) on itself and additional proteins such as histones and DNA repair factors.[6,7] Subsequently, PAR chains recruit other repair proteins and nucleic-acid-binding proteins. A recent study has reported that PARP1 quickly forms co-condensates with broken DNA via liquid-liquid phase separation (LLPS) and holds DNA ends in synapses.[8] Moreover, regulatory ubiquitination also triggers DSB signaling cascades and particularly induces local and global chromatin changes.[9] A network of posttranslational modifications orchestrates the DNA repair process.

DSB response and repair involve a variety of RNA-binding proteins (RBPs), RNA helicases, and ribonucleases.[10,11] These proteins may recruit DNA repair factors to DSB sites and modulate their activities.[12] Various species of RNA also participate in DSB repair. A set of long non-coding RNAs (lncRNAs) may serve as a scaffold for these RBPs and DDR factors or drive their phase separation at DNA damage sites. Moreover, upon DSB, the MRE11-RAD50-NBS1 complex recruits RNA polymerase II (Pol II), generating DNA damage-induced lncRNAs (dilncRNAs).[13] The processing, modification, and clearance of dilncRNAs require various mRNA/microRNA processing factors.[12,14,15] Subsequently, dilncRNAs promote LLPS of 53BP1 at DSB sites, which serves as a regulator of the DSB repair pathway choice.[15]

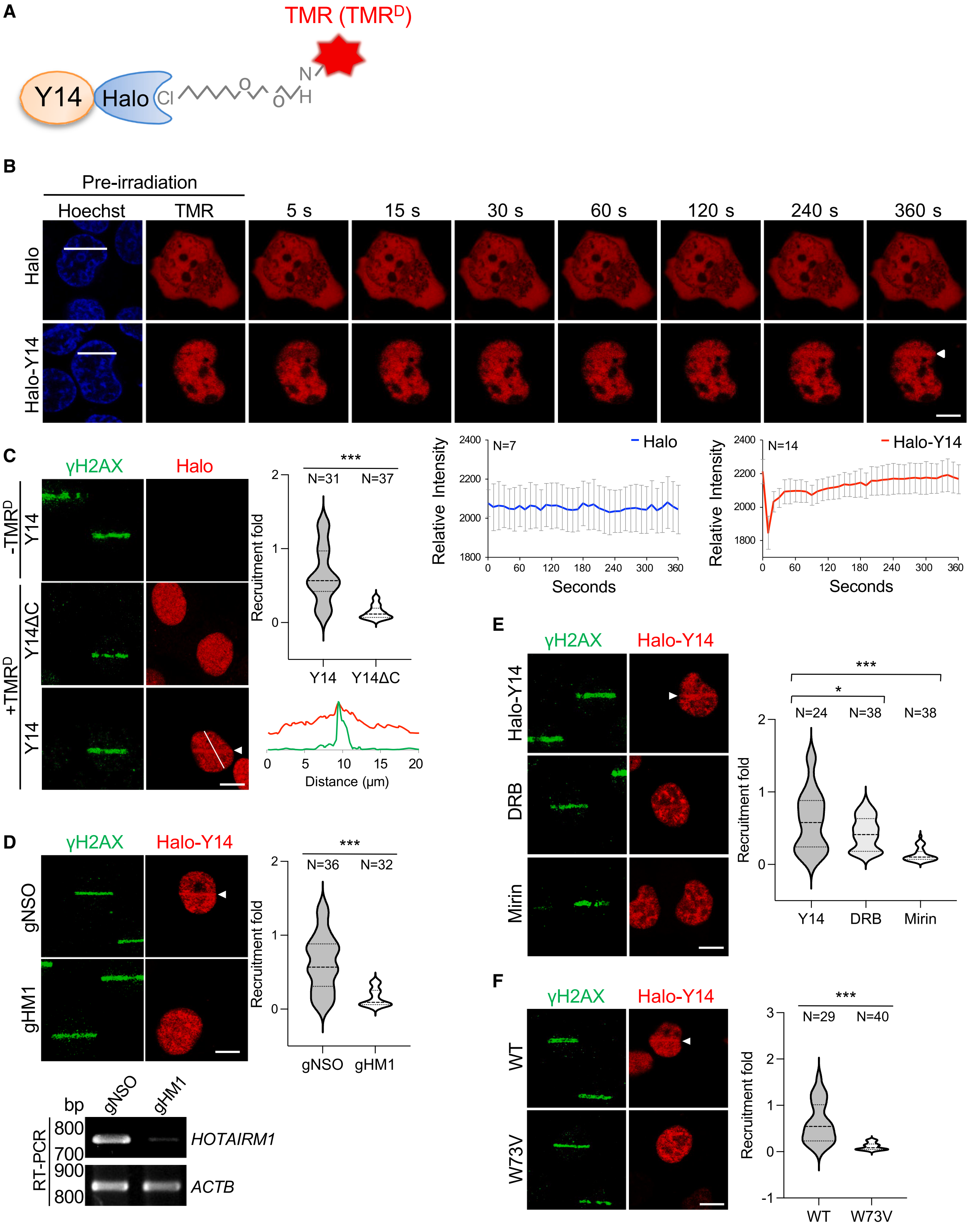

(legend on next page)

In addition, a set of RBPs directly interact with the repair machineries to regulate their activity. For example, the SFPQ/NONO heterodimer promotes DNA end joining mediated by the LIG4 and XRCC4 complex.[16] Several RBPs such as FUS and NONO localize to DSB sites in a PARP1-dependent manner.[17] FUS facilitates the recruitment of repair factors such as Ku80, NBS1, and 53BP1 and DNA end synapses via its phase-separated condensate formation.[18]

The roles of RBPs and distinct RNA species in DNA repair remain incompletely understood. The RBP Y14/RBM8A, known as a core component of the exon junction complex, participates in DSB repair via its RNA-mediated interaction with the NHEJ factors.[19] Y14-associated lncRNA *HOTAIRM1* recruits mRNA surveillance factors to degrade dilncRNAs at DSBs.[20] Moreover, Y14 contains the intrinsically disordered domains (IDRs) in its N- and C-terminal regions, which contribute to LLPS *in vitro.*[21] Both RNA binding and LLPS capacities of Y14 are essential for its activity in DNA repair.[21] However, our past studies detected only *HOTAIRM1* but not Y14 at laser-induced DNA damage sites.[20] Therefore, we attempted to investigate how Y14 acts at DNA lesions. This study led us to uncover phase-separated condensates of Y14 at DNA damage sites as well as their potential as a therapeutic target.

RESULTS

Localization of Y14 at DNA damage sites is dependent on RNA

Despite several lines of evidence indicating Y14's role in DSB repair,[19,20] we failed to observe endogenous Y14 or green fluorescent protein (GFP)-fusion Y14 at laser-induced DNA damage sites (Figure S1A). We suspected that Y14 at DNA damage sites may have been obscured by its abundance in the nucleus and that GFP may no longer fluoresce due to intense light exposure; other possibilities also remain. In this study, we took advantage of the self-labeling HaloTag, which can be visualized by cell-permeable fluorescent ligands (Figure 1A). Using a HaloTag ligand tetramethylrhodamine (TMR), we observed that transiently expressed Halo-Y14 was primarily localized in the nucleus of U2OS cells (Figure 1B, Halo-Y14, TMR). Live-cell microscopy revealed rapid accumulation of Halo-Y14 at laser-induced DNA damage sites (Figure 1B, Halo-Y14 images and line graph). Non-fusion Halo protein was distributed in both the nucleus and cytoplasm and was not accumulated at laser irradiation sites (Figure 1B, Halo). Therefore, the detection of Halo-Y14 signals at DSB sites was unlikely to be false positive. Immunofluorescence showed that laser-induced Halo-Y14 accumulation coincided with the distribution of γH2AX (Figure 1C, Y14+TMR^D). Truncation of the C-terminal domain abolished Y14 localization at DNA damage sites (Figure 1C, Y14ΔC). This observation reinforced the specific distribution of Y14 at DSB sites.

We have reported that Y14-associated lncRNA *HOTAIRM1* is localized at DNA damage sites.[20] *HOTAIRM1* depletion using a gapmer antisense oligonucleotide completely disrupted Y14 at DNA damage sites (Figure 1D, gHM1). Moreover, treatment of cells with the RNA Pol II inhibitor 5,6-dichlorobenzimidazole (DRB) diminished Y14 accumulation at the laser-induced strip (Figure 1E, DRB). Mirin, a potent MRE11 inhibitor, had the same effect as DRB (Figure 1E, Mirin). Quantitative reverse-transcription PCR confirmed the inhibitory effect of DRB and Mirin on dilncRNA expression (Figure S1B), as reported.[15] According to these observations, we deduced that Y14 is recruited by *HOTAIRM1*, and its stabilization at DNA damage sites may depend on DNA damage-induced dilncRNAs.[15] Moreover, the RNA-binding mutation W73V eliminated Y14 distribution at damage sites (Figure 1F), reinforcing its RNA-dependent colocalization with DSBs. These results provided the first line of evidence for Y14 localization at sites of DNA damage in an RNA-dependent manner.

Phosphorylation-dependent localization of Y14 at DNA damage sites

Halo tagging enabled us to explore how DNA damage signaling affects Y14 distribution. The C-terminal domain of Y14 contains duplicated arginine/serine (RS) dipeptides (Figure 2A), which are substantially phosphorylated in cells and can be phosphorylated by serine/arginine (SR) protein kinase 1 (SRPK1) *in vitro.*[22] It was not known whether SRPK1 phosphorylates Y14 in cells. Treatment of U2OS cells with the SRPK1 inhibitor SRPIN340 caused Y14 dephosphorylation. Using Phos-tag gel electrophoresis, we observed that SRPIN340 treatment accelerated Y14 migration (Figure 2B). Alkaline phosphatase-treated Y14 (Figure 2B) and non-phosphorylatable FLAG-tagged Y14SA (serine-to-alanine substitutions S166A and S168A, abbreviated as SA)[22] (Figure S2A) exhibited similar mobility to SRPIN340-treated Y14, indicating that phosphorylation of Y14 was effectively

Figure 1. RNA-dependent localization of Y14 at DNA damage sites

(A) Schematic diagram shows Halo-Y14 and its fluorescent ligands TMR (for live cells) and TMRDirect (TMR^D, for fixed cells).

(B) The Halo-Y14 expression vector was transiently transfected into U2OS cells. Laser microirradiation (LMI) coupled with live-cell fluorescence microscopy was performed in the presence of TMR. Images show pre-irradiated and post-irradiated cells (5–360 s). Hoechst staining shows the nuclei of pre-irradiated cells. Curve graphs show Halo (blue) or Halo-Y14 (red) dynamics at LMI strips ($N = 7$, Halo; $N = 14$, Halo-Y14). Panels B–F: Arrowhead denotes DNA damage sites induced by LMI.

(C) The empty or Halo-Y14 (wild type or ΔC) expression vector was transiently transfected into U2OS cells. TMR^D was used to detect Halo-Y14 in cells that were fixed 5 min post LMI. γH2AX was detected by indirect immunostaining using anti-γH2AX. Line-scan profiles show fluorescence and γH2AX intensity along a white line.

(D) The Halo-Y14 vector was cotransfected with non-specific control (gNSO) or HOTAIRM1 (gHM1) gapmer into U2OS cells. HOTAIRM1 and β-actin mRNA (ACTB as control) were detected by RT-PCR.

(E) U2OS cells that transiently expressed Halo-Y14 were mock treated or treated with DRB or Mirin. ($^*p < 0.05$; $^{***}p < 0.001$)

(F) Halo-Y14 (wild type or W73V) was transiently expressed in U2OS cells.

(D–F) LMI and staining of Halo-Y14 and γH2AX were as in (C). Scale bar in all images: 20 μm. Violin plots of (C)–(F) show fold recruitment of Halo-Y14 (Y14ΔC) to laser-induced DNA damage sites (details in STAR Methods); the number (N) of cells for measurement ($^{***}p < 0.001$).

See also Figure S1.

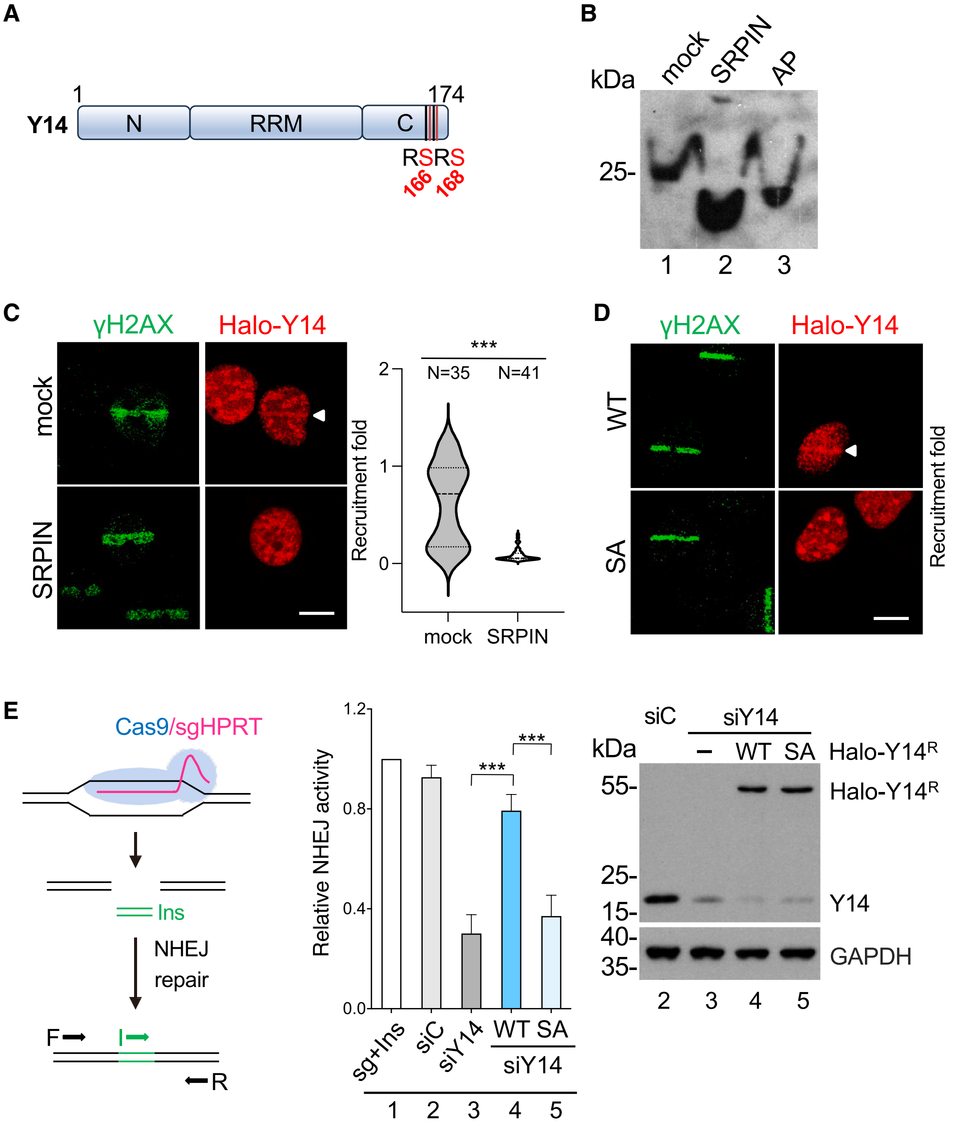

Figure 2. Phosphorylation-dependent localization of Y14 at DNA damage sites

(A) Diagram shows the domain structure of Y14 and its phosphorylation sites.[22]

(B) U2OS cells were mock treated (lanes 1 and 3) or treated with SRPIN340 (lane 2). Mock lysates were untreated (lane 1) or treated with alkaline phosphatase (lane 3, AP). Lysate proteins were fractionated on a Phos-tag gel, followed by immunoblotting using anti-Y14.

(C) U2OS cells were transfected with the Halo-Y14 vector and then mock treated or treated with SRPIN340 for 48 h. For both (C) and (D), LMI and staining of Halo-Y14 and γH2AX were as in Figure 1C (scale bar: 20 μm). Violin plots of (C) and (D) show fold recruitment of Halo-Y14 to LMI sites as in Figure 1.

(D) U2OS cells were transfected with the Halo-Y14 vectors (wild type or SA).

(E) Diagram shows the repair assay for Cas9/sgRNA-induced DSBs.[20] Upon cotransfection with the Cas9/sgHPRT vector, the Ins dsDNA oligonucleotide can be inserted into cleaved DNA. F, I, and R represents PCR primers. For the repair assay, U2OS cells were transfected with the Cas9/sgHPRT vector and Ins (lanes 1–5). Additional vectors transfected included siRNA control (lane 2, siC), siY14 (lanes 3–5), or siY14-resistant Halo-Y14 (lane 4 for wild type, and lane 5 for SA). Relative NHEJ activity was measured by I-R/F-R (lane 1 was set to 1; mean ± SD; $N = 3$; ***$p < 0.001$ for a two-tailed test). Immunoblotting was performed using antibodies against Y14 and GAPDH (the lane number was the same as in the bar graph).

See also Figure S2.

abolished by SRPIN340. Using laser microirradiation (LMI), we observed that Halo-Y14 localization at laser-induced tracks was abolished by SRPIN340, while γH2AX was not affected (Figure 2C). Similarly, Halo-Y14SA was unable to localize to DNA damage sites (Figure 2D). Inhibition of any DDR kinase (DNA-PK, ATM, or ATR) also impaired Halo-Y14 accumulation at DSBs in U2OS cells (Figure S2B). Despite slight differences across cell lines, DDR kinase inhibitors neither significantly altered cellular distribution of SRPK1 nor reduced Y14 phosphorylation in U2OS cells (Figures S2C and S2D), suggesting that DDR kinases affect Y14 recruitment to DSBs via other factors. Using a repair assay for Cas9-induced DSBs,[20] we

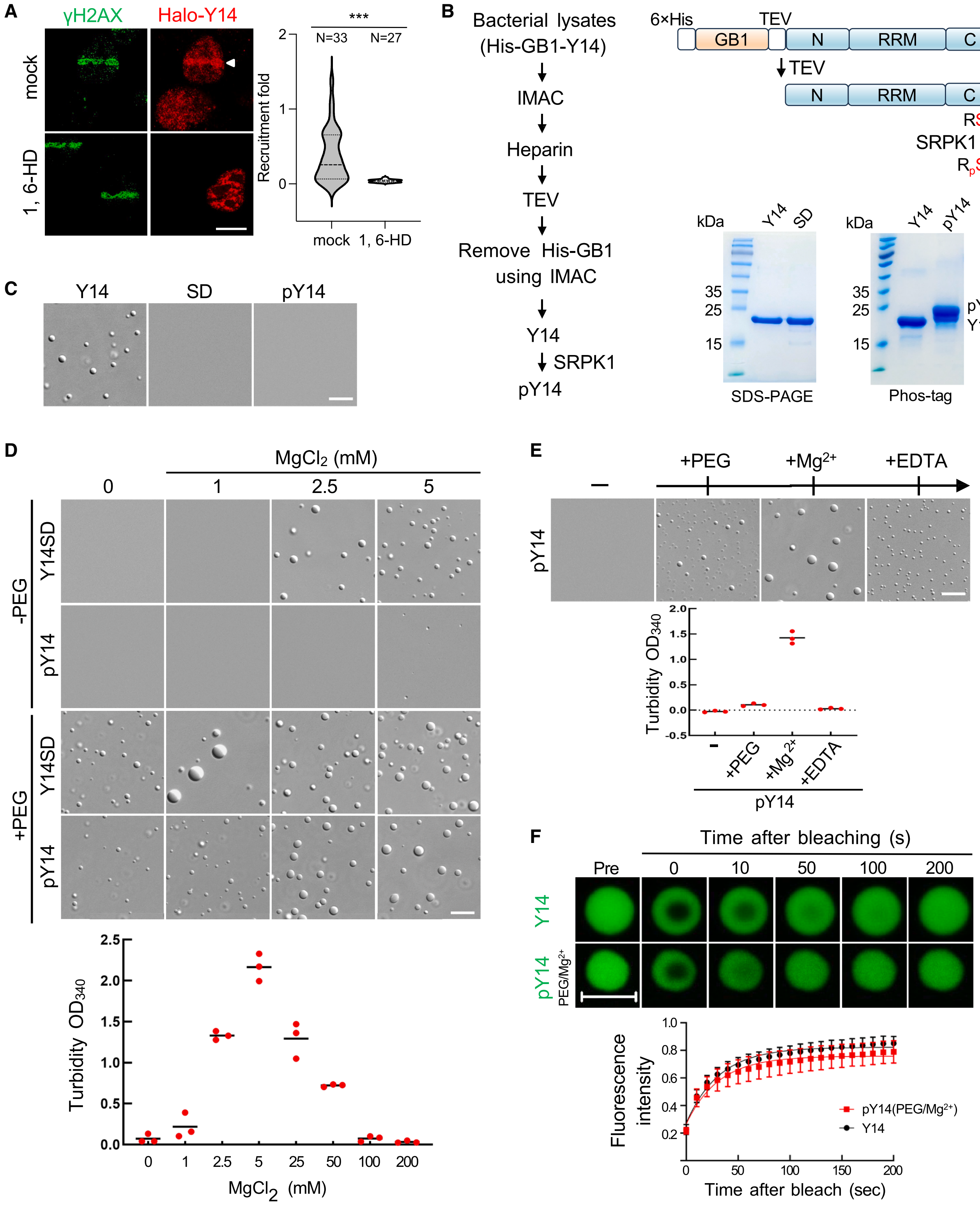

Figure 3. Mg^{2+} promotes phase separation of phosphorylated Y14

(A) U2OS cells were transiently transfected with the Halo-Y14 vector followed by mock or 1,6-HD treatment. LMI and detection of Halo-Y14 and γH2AX were as in Figure 1C (scale bar: 20 μm). A violin plot is shown as in Figure 1.

(legend continued on next page)

demonstrated that Halo-Y14 could restore the DSB repair activity in Y14-depleted cells, whereas the Y14SA mutant could not (Figure 2E). This result demonstrated that Halo-Y14 was functional. Moreover, SRPK1-mediated phosphorylation of Y14 was critical for its localization to DNA lesions and function in DSB repair.

Phase separation of phosphorylated Y14 requires magnesium

Several DDR factors such as FUS, 53BP1, and MDC1 form DNA repair compartments via phase separation.[18,23,24] The detection of Y14 at DNA damage sites prompted us to test whether phase separation plays a role in Y14 condensation. 1,6-hexanediol (1,6-HD) can disrupt membraneless condensates formed by LLPS.[25] We observed that 1,6-HD treatment abolished Halo-Y14 localization at laser-induced tracks (Figure 3A), suggesting phase separation of Y14 at DNA lesions. We have previously reported that recombinant Y14 with S- and His-tags undergoes reversible LLPS to form liquid-like droplets *in vitro.*[21] However, non-phosphorylated Y14 was used in that study. To determine whether phosphorylation affects LLPS, it was necessary to examine phosphomimetic or phosphorylated Y14. Moreover, to avoid non-specific effects of the fusion tags, we used untagged Y14 in this study (Figure 3B, see STAR Methods). In brief, we purified recombinant Y14 containing His-tagged protein G B1 domain (GB1) and then removed His-GB1 using the tobacco etch virus (TEV) protease (Figure 3B). Non-tagged Y14 formed spherical droplets around pH 7.2 (Figure 3C), and its droplets tended to cling to each other at lower pH (Figure S3A). Next, we generated a phosphomimetic mutant of Y14 (S166, 168D, abbreviated as SD) and phosphorylated Y14 *in vitro* using SRPK1.[22] We confirmed the phosphorylation status of phosphorylated Y14 (pY14) using Phos-tag gel (Figure 3B). However, neither Y14SD nor pY14 phase separated (Figure 3C) regardless of pH (Figure S3A).

Duplicated RS dipeptides in Y14 are similar to SR proteins, a group of splicing factors with RS dipeptides in varying numbers.[26] Since magnesium can precipitate SR proteins by interacting with phosphorylated RS dipeptides,[27] we tested its effects on LLPS of Y14SD and pY14. We initially observed that 1 mM Mg^{2+} induced 20 μM Y14SD to form droplets at the edges of the solution on microscope slides (Figure S3B, Y14SD/1 mM Mg^{2+}). As Mg^{2+} concentration increased, droplets were evenly distributed throughout the solution and gradually diminished at the edges (Figures 3D, S3B, and S3C, 20 μM Y14SD/2.5 and 5 mM Mg^{2+}). Using 20 μM pY14, we observed that Mg^{2+}-induced droplets accumulated only at the edges (Figures S3B and S3C, 20 μM pY14/2.5 and 5 mM Mg^{2+}). Nevertheless, 3% PEG promoted even distribution of pY14 droplets, and Mg^{2+} further enhanced droplet formation (Figure 3D, pY14/+PEG). PEG also lowered Mg^{2+} concentration thresholds for Y14SD (Figure 3D, Y14SD/+PEG). Addition of EDTA to Mg^{2+}/PEG-induced pY14 droplets substantially reduced their size, indicating Mg^{2+}-mediated LLPS (Figure 3E). Nevertheless, higher concentrations (25–200 mM) of Mg^{2+} suppressed pY14 droplet formation (Figure 3D, turbidity). Fluorescence recovery after photobleaching (FRAP) experiment showed that the fluidity of pY14 in PEG/Mg^{2+}-induced droplets was similar to that of Y14 in crowder-free droplets (Figure 3F). Together, these results revealed Mg^{2+}-mediated pY14 phase separation.

Y14 condensates recruit Ku70/80 via phase separation

Biomolecules with a high capacity for phase separation can act as a scaffold to recruit client molecules.[28] Since Y14 facilitates the recruitment of Ku70/80 to laser-induced DNA lesions,[19] we tested whether such recruitment involves heteromolecular phase separation. Using Alexa Fluor 488-labeled Ku70/80 heterodimer, we observed a partitioning of Alexa Fluor 488-labeled Ku70/80 heterodimer into pY14 droplets (Figure 4A, mock). EDTA dissolved such heterotypic Y14-Ku70/80 droplets (Figure 4A, +EDTA). CIDER analysis[29] (https://pappulab.wustl.edu/CIDER/) revealed that Ku70 and Ku80 each have two IDRs with varying amounts of charged residues (Figure S3D). Net charge per residue (NCPR) analysis[29] indicated that the Ku70-2 IDR has a net positive charge, although near-zero (NCPR = 0.037), whereas all other IDRs have a net negative charge (Figure S3D). For the LLPS assay, two Ku70 IDRs were selected due to their different properties and charge distributions. The N-terminal IDR of Ku70 (Ku70-1) was the most negatively charged one (NCPR = −0.357) among all the IDRs (Figure S3D). The Ku70-2 IDR between the DNA-binding domain and the SAF-A/B, Acinus, and PIAS (SAP) domain is remarkably similar to the N-terminal domain of Y14, which features alternating charge stretches.[21] An IDR of the endonuclease Artemis, containing only one basic residue (Figures 4B and S3D, NCPR = −0.045), was used for comparison in the LLPS assay (see the following paragraph).

Using TAMRA-labeled peptides as clients, we found that Ku70-2 partitioned more efficiently into PEG/Mg^{2+}-induced pY14 droplets than Ku70-1 (Figure 4B, Ku70-1 and Ku70-2). The

---

(B) Flow chart shows purification of His-GB1-Y14 and subsequent phosphorylation of non-tagged Y14. Schematic diagram shows the domain structure of His-GB1-Y14 and non-tagged Y14 (wild type and SD). SRPK1 phosphorylates S166 and S168 of wild-type Y14.[22] SDS-PAGE shows purified Y14 and Y14SD, and Phos-tag gel for Y14 and pY14.

(C) Representative images of differential interference contrast (DIC) microscopy show LLPS of Y14, Y14SD, and pY14. Scale bar in (C)–(E): 10 μm.

(D) Representative DIC images show the effect of increasing Mg^{2+} concentrations on LLPS of Y14SD and pY14 without or with 3% PEG. Turbidity at 340 nm was measured for Mg^{2+}/PEG-induced pY14 LLPS.

(E) LLPS of pY14 was performed in the absence (−) of PEG and Mg^{2+}. Subsequently, 3% PEG, 2.5 mM Mg^{2+}, and 2 mM EDTA were sequentially added. Turbidity was measured as in (D).

(F) Fluorescent images and graph show the recovery kinetics of FRAP analysis of Y14 in the absence PEG/Mg^{2+} and pY14 in the presence of 3% PEG and 2.5 mM $MgCl_2$. FRAP curves show Alexa 488 fluorescence dynamics over a 200-s period.

The curves were fitted by one-phase exponential equations (see STAR Methods). The average fluorescence before bleaching was set to 1 (mean ± SD). Scale bar: 5 μm.

See also Figure S3.

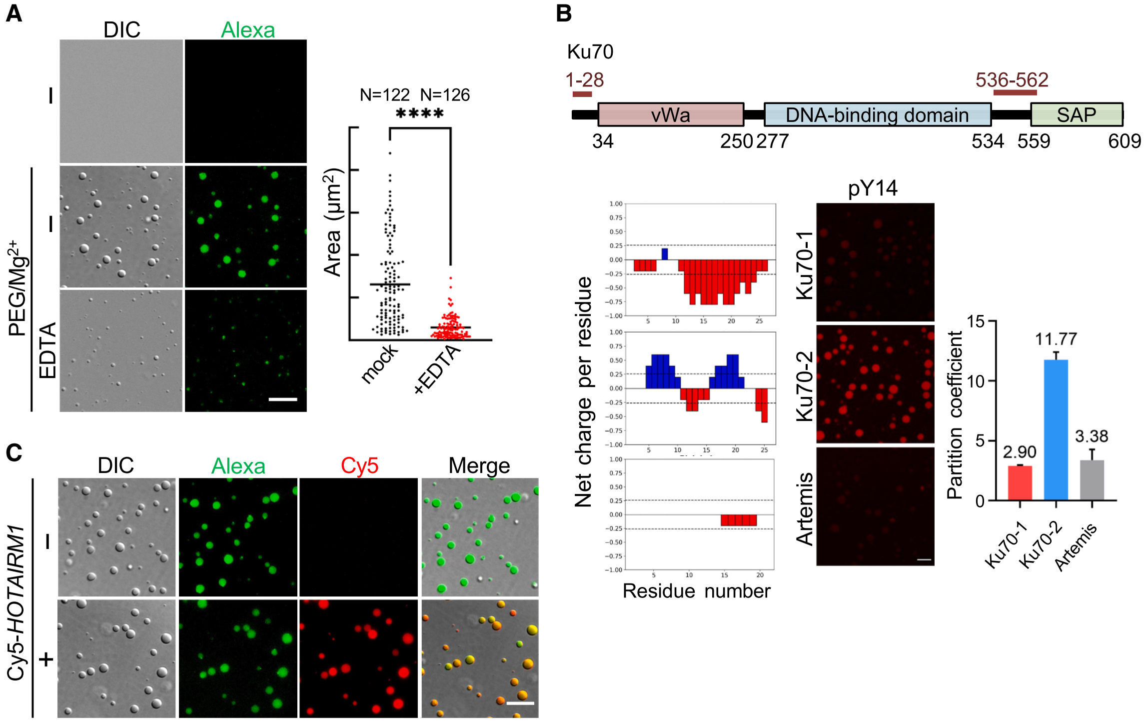

Figure 4. Partitioning of Ku70/80 into phase-separated pY14 droplets

(A) Alexa 488-labeled Ku70/80 heterodimer was incubated with pY14 in the absence (–) or presence (+) PEG and Mg^{2+}. The latter was then treated with EDTA as in Figure 3E. Left and right: DIC and fluorescence imaging (Alexa). Dot plots show pY14-Ku70/80 droplet sizes in the absence and presence of EDTA ($N = 122$ and 126; ****$p < 0.0001$).

(B) Schematic diagram shows the domain structure of Ku70. Two IDR peptides (1 and 2) are indicated. Net charge per residue (NCPR) profile along the linear sequence of the indicated peptides was obtained by CIDER (see STAR Methods); blue and red indicate positive and negative charges, respectively. TAMRA-labeled IDR peptides were each incubated with pY14 in the presence of PEG and Mg^{2+}. Bar graph shows the partition coefficient of the IDR peptides (mean ± SD).

(C) Partitioning of Alexa 488-labeled Ku70/80 into Mg^{2+}/PEG-induced pY14 droplets in the absence (–) or presence (+) of Cy5-labeled *HOTAIRM1.* Scale bar in all images: 10 μm.

See also Figure S3.

Artemis IDR failed to partition into pY14 droplets (Figure 4B, Artemis). Consistently, far-western blot analysis showed that Ku70-2 had a greater affinity for immobilized pY14 than for the two other peptides (Figure S3E), suggesting the potential interaction between Y14 and Ku70-2. This observation was reminiscent of our previous finding that positively charged residues in Y14 IDRs play a greater role in its LLPS than residues with negative charges.[21] This result suggested that heterotypic Y14-Ku70/80 LLPS may involve electrostatic interactions that favor IDRs containing basic residues. RNA can co-phase separate with Y14[21] and was required for Y14 localization at DNA damage sites (Figure 1). Using Cy5-labeled *HOTAIRM1*, we observed that it co-phase separated with Y14 and Ku70/80 (Figure 4C). Together, Y14 recruited Ku70/80 via charged IDR-mediated LLPS to form ribonucleoprotein condensates.

NHEJ factors localize to DNA damage sites in an EDTA-sensitive manner

Mg^{2+}-dependent pY14 LLPS prompted us to test whether Y14 localization at DNA damage sites requires Mg^{2+}. We treated cells with cell-permeant EDTA-acetoxymethyl ester (EDTA-AM) to chelate divalent cations and observed that it disrupted laser-induced Halo-Y14 strips (Figure 5A), suggesting that divalent cations are required for Y14 concentration at DNA damage sites. Y14 recruits Ku70/80 to DNA damage sites.[19] Therefore, we explored whether localization of Ku70/80 and other NHEJ factors at DNA lesions is divalent cation dependent. First, we examined their distribution at laser-induced strips in Y14-depleted cells. Consistent with our previous observation,[19] Y14 depletion reduced Ku70 accumulation (Figure 5B, Ku70). Similarly, Y14 depletion also compromised DNA damage site localization of DNA-PKcs, LIG4, and XLF (Figure 5B, DNA-PKcs, LIG4, and XLF). In contrast, Y14 depletion has no significant effect on PAR polymer or FUS accumulation at DSB sites (Figure 5B, PAR and FUS). Meanwhile, we examined whether the distribution of the aforementioned factors to DSB sites is sensitive to divalent cation chelation. EDTA-AM treatment substantially reduced the level of NHEJ core factors (Ku70, DNA-PKcs, LIG4, and XLF) at laser-induced DNA damage sites but had no significant effects on PAR polymers and FUS (Figure 5C). Therefore, Mg^{2+}-dependent Y14 condensate formation may contribute to NHEJ factor recruitment to DSB sites. Finally, EDTA-AM did not further reduce Ku70 recruitment in Y14-depleted cells (Figure S4), suggesting that Y14 is the major factor sensitive to EDTA at DSBs.

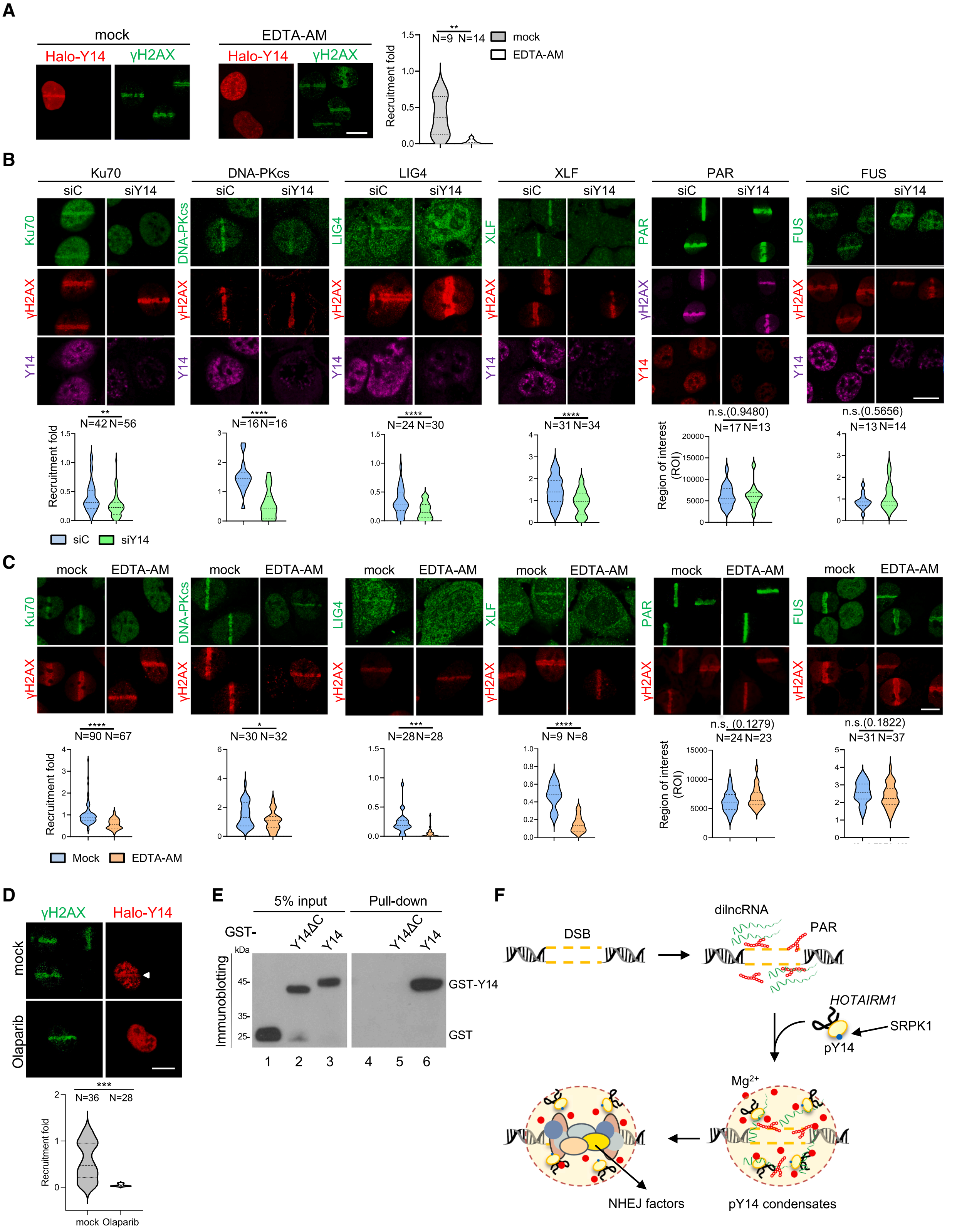

(legend on next page)

Since PARP1 acts as a DNA damage sensor and rapidly detects DNA lesions[6,8,30] and its association with DSBs was independent of Y14 or insensitive to EDTA-AM (Figures 5B and 5C), we inversely examined whether inhibition of PARP1 affects Y14 condensates at DSB sites. Treatment of cells with the PARP1 inhibitor olaparib abolished Halo-Y14 accumulation at DNA damage strips (Figure 5D). Using biotin-PAR and streptavidin affinity selection, we observed that recombinant full-length GST-Y14 but not GST or C-terminally truncated Y14 bound PAR polymers (Figure 5E). Therefore, our results established a model suggesting that Y14 is recruited to DSBs upon PARP1 activation and its phosphorylation renders Mg^{2+}-dependent condensate formation, which further promotes the recruitment of NHEJ factors (Figure 5F).

SRPK1 inhibition impairs DSB repair and enhances cellular sensitivity to DNA damage

Our initial finding for the localization of phosphorylated Y14 at DSB sites (Figure 2) led us to uncover Mg^{2+}-dependent Y14 LLPS (Figure 3). Although EDTA-AM significantly reduced the recruitment of NHEJ factors to DSBs (Figure 5), it may interfere with multiple cellular processes. Therefore, we tested whether inhibition of SRPK1 causes a similar effect to Mg^{2+} chelation. As a result of SRPIN340 treatment, Ku70/80 recruitment to laser-induced DSBs was significantly reduced, while the accumulation of PAR chains was not affected (Figure 6A). Moreover, SRPK1 inhibition also reduced the repair activity for Cas9-induced DSBs by 30% (Figure 6B). Accordingly, SRPIN340 treatment induced γH2AX in U2OS (Figure 6C), indicating that inhibition of SRPK1 led to the accumulation of DNA damage. Next, we evaluated whether SRPIN340 also influences the radiosensitivity and chemosensitivity of U2OS cells *in vitro*. Cell proliferation and colony formation were gradually reduced by increasing the doses of ionizing irradiation (IR) or the DNA-damaging agent camptothecin (CPT) (Figure 6D for proliferation; Figures 6E and S5A for colony formation). The combination of SRPIN340 with IR or CPT resulted in a dose-dependent increase in cytotoxicity (Figures 6D, 6E, and S5A). Similar results were observed in HeLa cells (Figures S5B and S5C). Therefore, SRPK1 inhibition enhanced cellular sensitivity to DNA damage, suggesting that targeting Y14 condensates at DNA damage sites is a strategy for combinational anticancer therapy.

DISCUSSION

This study revealed RNA- and phosphorylation-dependent recruitment of Y14 to DNA damage sites. We then found that Mg^{2+} promoted phase separation of phosphorylated Y14 *in vitro* and its localization at damaged sites. Y14 condensates at DNA lesions further recruit a set of NHEJ factors. Disruption of Y14 condensates reduced DNA repair efficiency and enhanced anticancer activity of DNA damage reagents.

Y14 localization at DNA damage sites depends on RNA and PARP1 activation

Using HaloTag fusion, we observed Y14 at DNA damage sites. In comparison with endogenous or GFP-fusion proteins, HaloTag-ligand complexes may withstand laser irradiation and cell fixation. During this study, we also learned that HaloTag has been used to determine the dynamics of DDR and NHEJ protein recruitment at DSBs.[31,32] The distribution of Y14 to LMI-induced DNA damage sites exhibited similar kinetics to that of the NHEJ factors.[32] In addition, our result revealed that *HOTAIRM1* was essential for Y14 recruitment (Figure 1), reinforcing the role of this lncRNA in DNA damage repair. Moreover, inhibition of RNA Pol II or PARP1 impaired Y14 localization at DSBs (Figures 1 and 5), suggesting that dilncRNAs and PAR polymers may recruit or stabilize Y14 at DSBs or provide multivalent molecular interactions for Y14 and other RBPs. As a result of their respective loss of binding ability to RNA and PAR, the W73V and ΔC mutants of Y14 no longer localized at DSBs. Overall, Y14, like FUS,[18,33] formed condensates at DSBs in part via association with RNA and PAR chains.

EDTA-sensitive recruitment of DNA repair factors

Y14 has a minimal phosphorylated RS domain that binds Mg^{2+}.[34] Our results showed that Mg^{2+} promoted *in vitro* LLPS of pY14, and EDTA abolished the localization of Y14 at DSB sites (Figures 3 and 5). Mg^{2+} is an abundant divalent cation in cells, with approximately 15–25 mM present.[35] Since phase separation of pY14 *in vitro* required only a few millimolars of Mg^{2+}, physiological Mg^{2+} levels may be sufficient. Mg^{2+}-dependent phase separation of pY14 was reminiscent of that of the nucleosomes.[36] LLPS of the nucleosomes can also be tuned by post-translational modification.[37] Notably, EDTA also impaired the recruitment of NHEJ core factors to DSBs, which consistently exhibited Y14 dependency (Figure 5). In contrast, FUS recruitment and PAR polymerization likely occurred before Y14 accumulation at DSBs. PARP1 activation and RNA Pol II transcription are the earliest events in DSB repair process.[7,13] PAR and dilncRNAs may facilitate the recruitment or stabilization of Y14 at DSBs (Figure 5F). Subsequently, Mg^{2+}-dependent pY14

Figure 5. Chelation of divalent cations impairs the recruitment of the NHEJ factors to DNA damage sites

(A) U2OS cells that transiently expressed Halo-Y14 were mock treated or treated with EDTA-AM. LMI and staining of Halo-Y14 or γH2AX was as in Figure 1C. Scale bar in (A)–(D): 20 μm.

(B) U2OS cells were transfected with siC or siY14, followed by LMI and indirect immunofluorescence of indicated NHEJ factors, PAR, or FUS.

(C) U2OS cells were mock treated or treated with EDTA-AM, followed by LMI and indirect immunofluorescence as in (B). Violin plots are shown as in (B).

(D) U2OS cells that transiently expressed Halo-Y14 were mock treated or treated with olaparib. LMI and staining were as in (A).

(E) Purified GST and GST-Y14 were subjected to the PAR pull-down assay. Input (5%) and pull-down were immunoblotted using anti-GST.

(F) Model for the role of Y14 at DNA damage sites. Y14 localized to DNA damage sites in an *HOTAIRM1*- and phosphorylation-dependent manner. PAR chains and dilncRNAs may also facilitate Y14 localization at DSBs. Mg^{2+} (or other divalent cations) promotes phase separation of pY14 and subsequent recruitment of NHEJ factors for DSB repair.

For (A)–(D), violin plots show fold recruitment of Halo-Y14 or other indicated factors to LMI sites as in Figure 1; the number (N) of cells for measurement and p values are indicated (****$p < 0.0001$; ***$p < 0.001$; **$p < 0.01$; *$p < 0.05$; n.s. represents not significant; p value indicated in parentheses).

See also Figure S4.

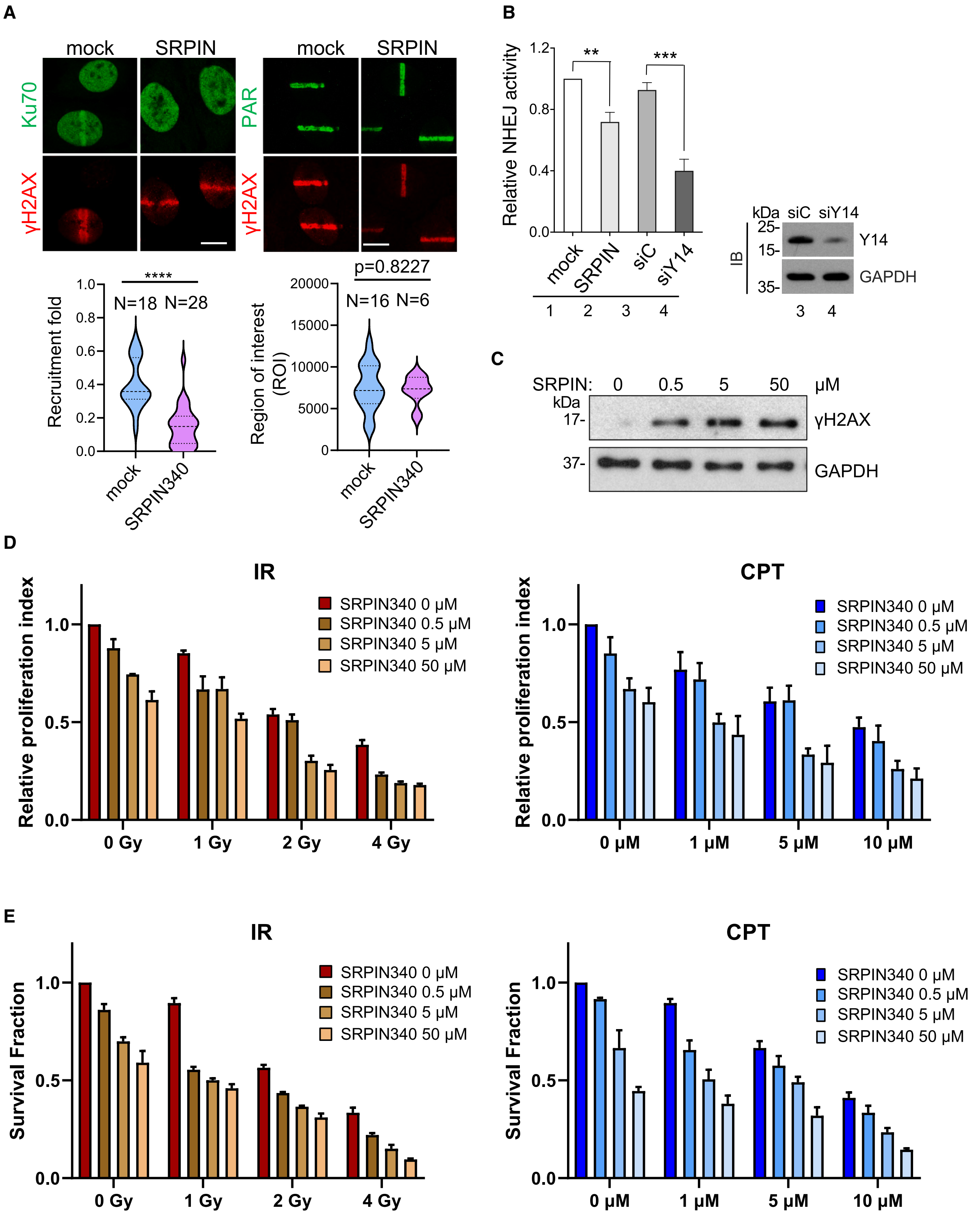

(legend on next page)

condensates may increase local concentrations of Ku70/80 at DSBs through electrostatic interaction-mediated LLPS. Whether the remaining NHEJ factors partition into Y14 condensates via LLPS or they are recruited by Ku70/80 through specific interactions was not tested. Moreover, whether the phosphorylation status of Y14 is tuned during DNA repair and hence influences its condensates also remains to be answered.

Inhibition of SRPK1 abolishes Y14 condensates and DSB repair

Using an SRPK1 inhibitor, we found that phosphorylation of Y14's RS dipeptides was essential for its localization at DSBs (Figure 2). Consistently, the SA mutation abolished Y14 localization at DSBs. Indeed, a large portion of Y14 is phosphorylated in cells.[22] Therefore, it is possible that SRPK1 constitutively phosphorylates Y14, regardless of DNA damage. Inhibition of DDR kinases also impaired localization of Y14 at DSBs (Figure S2B). It has been reported that DDR kinases promote nuclear translocation of SRPK1 in response to certain DNA-damaging agents.[38] However, neither LMI nor DDR kinase inhibitors significantly affected subcellular distribution of SRPK1 (Figure S2C), leading us to speculate that DDR kinases might indirectly influence Y14 localization at DSBs. Importantly, we found that inhibition of SRPK1 reduced Ku70/80 recruitment, compromised DNA repair efficiency, and enhanced the cytotoxicity of IR and CPT to cancer cells (Figure 6). Therefore, it may be possible to selectively target cancers with defective DNA repair by inhibiting Y14 phosphorylation. Moreover, targeting the condensates of DNA repair factors has been considered a new strategy for cancer treatment.[23,39] Accordingly, disruption of Y14 condensates could be therapeutically beneficial.

This study reports that Y14 accumulates at DSBs upon PARP1 activation and recruits NHEJ factors via LLPS. Y14 likely serves as a multivalent integrator that coordinates RNA, Mg^{2+}, and PARP1 signaling for DNA repair, and its phosphorylation-dependent condensation makes it an attractive drug target for anticancer treatment.

Limitations of the study

The use of HaloTag enabled our detection of Y14 condensates at DSB sites. However, with overexpressed Halo-Y14, false-positive results cannot be completely excluded. Therefore, the generation of endogenous Halo-Y14 via genomic editing will be beneficial for future research. Although Mg^{2+} promoted *in vitro* LLPS of Y14 and EDTA disrupted Halo-Y14 condensates in cells, it is yet unclear whether other divalent cations act as Y14 LLPS drivers or how their concentration is tuned at DSB sites. Moreover, treatment with ion chelators or SRPK1 inhibitors is likely to impair multiple cellular processes, rather than only preventing DNA repair foci from forming.

RESOURCE AVAILABILITY

Lead contact

Further information and requests for resources and reagents should be directed to and will be fulfilled by the lead contact, Woan-Yuh Tarn (wtarn@ibms.sinica.edu.tw).

Materials availability

There are restrictions on the availability of new generated plasmids due to MTA.

Data and code availability

- All data reported in this article will be shared by the lead contact upon request.
- This article does not report original code.
- Any additional information required for analysis of the data reported in this article is available from the lead contact upon request.

ACKNOWLEDGMENTS

We thank the Light Microscopy Core Facility and DNA Sequencing Core Facility of the Institute of Biomedical Sciences, Academia Sinica. The core facility is funded by Academia Sinica Core Facility and Innovative Instrument Project (AS-CFII-113-A12). This work was supported by Academia Sinica (AS-TP-113-L05) to W.-Y.T.

AUTHOR CONTRIBUTIONS

C.-H.S., T.-W.C., and H.-H.Y. contributed equally to the design and execution of experiments. C.-H.S. examined the recruitment of NHEJ factors (Figures 2B, 5A–5C, 6A, S2A, and S4). T.-W.C. examined the localization of Y14 at DNA damage sites and DSB repair assay (Figures 1, 2, 5D, 5E, 6B, S1, and S2B–S2D). H.-H.Y. performed *in vitro* LLPS assays (Figures 3, 4, and S3). C.-L.S. examined cell viability and colony formation (Figures 6C–6E and S5). P.-Y.H. performed Phos-tag gel electrophoresis for pY14 (Figures 3B and S3E). Y.L. designed and constructed the HaloTag expression vector. W.-Y.T. conceived the study, supervised the experiments, and wrote and revised the manuscript.

DECLARATION OF INTERESTS

The authors declare no competing interests.

STAR★METHODS

Detailed methods are provided in the online version of this paper and include the following:

- KEY RESOURCES TABLE
- EXPERIMENTAL MODEL AND STUDY PARTICIPANT DETAILS

Figure 6. SRPK1 inhibition impairs DSB repair and enhances cellular sensitivity to DNA damage
(A) U2OS cells were mock treated or treated with SRPIN340 for 48 h. LMI was performed, followed by indirect immunofluorescence using antibodies against Ku70, γH2AX, and PAR. Violin plots are shown as in Figures 5B and 5C. Scale bar: 20 μm.
(B) For the DSB repair assay, U2OS cells transfected with the Cas9/sgRNA vector and Ins dsDNA oligonucleotide were either mock treated or treated with SRPIN340 for 48 h (lanes 1 and 2). For comparison, U2OS were transfected with Cas9/sgRNA, Ins, and siC or siY14 as in Figure 2E (lanes 3 and 4). Bar graph shows qPCR, representing the repair efficiency (mean ± SD; $N = 3$; ***$p < 0.001$ and **$p < 0.01$ for a two-tailed test).
(C) U2OS cells were treated with different concentrations of SRPIN340. Immunoblotting of γH2AX was shown; GAPDH was as loading control.
(D) U2OS cells were treated with different doses of SRPIN340 for 24 h and then exposed to different doses (Gy) of IR (left) or camptothecin (CPT) (right). After treatment, cell proliferation was measured using the CCK-8 assay.
(E) U2OS cells were treated as in (C), followed by the colony formation assay. (D and E) Three independent repeats were performed for quantification.
See also Figure S5.

- Cell lines and cell cultures
- METHOD DETAILS
  - Plasmid construction
  - Cell culture, transfection, and drug treatment
  - Laser microirradiation and fluorescence imaging
  - Immunoblotting
  - Purification of recombinant non-tagged Y14 protein
  - *In vitro* phosphorylation of recombinant Y14
  - Phos-tag gel electrophoresis
  - Fluorescent labeling of proteins
  - *In vitro* transcription and Cy5-labeling of RNA
  - Liquid-liquid phase separation (LLPS) assay
  - Fluorescence recovery after photo bleaching (FRAP)
  - Turbidity measurements
  - Far-western blot analysis
  - Nonhomologous end joining (NHEJ) assay
  - RT-PCR and qPCR
  - PAR binding assay
  - Cell proliferation assay
  - Colony formation assay
- QUANTIFICATION AND STATISTICAL ANALYSIS

SUPPLEMENTAL INFORMATION

Supplemental information can be found online at https://doi.org/10.1016/j.isci.2025.113073.

Received: March 31, 2025
Revised: May 27, 2025
Accepted: July 3, 2025
Published: July 7, 2025

REFERENCES

1. Lieber, M.R. (2010). The mechanism of double-strand DNA break repair by the nonhomologous DNA end-joining pathway. Annu. Rev. Biochem. *79*, 181–211. https://doi.org/10.1146/annurev.biochem.052308.093131.
2. Stinson, B.M., and Loparo, J.J. (2021). Repair of DNA double-strand breaks by the nonhomologous end joining pathway. Annu. Rev. Biochem. *90*, 137–164. https://doi.org/10.1146/annurev-biochem-080320-110356.
3. Aymard, F., Bugler, B., Schmidt, C.K., Guillou, E., Caron, P., Briois, S., Iacovoni, J.S., Daburon, V., Miller, K.M., Jackson, S.P., and Legube, G. (2014). Transcriptionally active chromatin recruits homologous recombination at DNA double-strand breaks. Nat. Struct. Mol. Biol. *21*, 366–374. https://doi.org/10.1038/nsmb.2796.
4. Giglia-Mari, G., Zotter, A., and Vermeulen, W. (2011). DNA damage response. Cold Spring Harb. Perspect. Biol. *3*, a000745. https://doi.org/10.1101/cshperspect.a000745.
5. Blackford, A.N., and Jackson, S.P. (2017). ATM, ATR, and DNA-PK: the trinity at the heart of the DNA damage response. Mol. Cell *66*, 801–817. https://doi.org/10.1016/j.molcel.2017.05.015.
6. Ray Chaudhuri, A., and Nussenzweig, A. (2017). The multifaceted roles of PARP1 in DNA repair and chromatin remodelling. Nat. Rev. Mol. Cell Biol. *18*, 610–621. https://doi.org/10.1038/nrm.2017.53.
7. Alemasova, E.E., and Lavrik, O.I. (2019). Poly(ADP-ribosyl)ation by PARP1: reaction mechanism and regulatory proteins. Nucleic Acids Res. *47*, 3811–3827. https://doi.org/10.1093/nar/gkz120.
8. Chappidi, N., Quail, T., Doll, S., Vogel, L.T., Aleksandrov, R., Felekyan, S., Kühnemuth, R., Stoynov, S., Seidel, C.A.M., Brugués, J., et al. (2024). PARP1-DNA co-condensation drives DNA repair site assembly to prevent disjunction of broken DNA ends. Cell *187*, 945–961.e18. https://doi.org/10.1016/j.cell.2024.01.015.
9. Kolobynina, K.G., Rapp, A., and Cardoso, M.C. (2022). Chromatin ubiquitination guides DNA double strand break signaling and repair. Front. Cell Dev. Biol. *10*, 928113. https://doi.org/10.3389/fcell.2022.928113.
10. Kai, M. (2016). Roles of RNA-binding proteins in DNA damage response. Int. J. Mol. Sci. *17*, 604. https://doi.org/10.3390/ijms17040604.
11. Klaric, J.A., Wüst, S., and Panier, S. (2021). New faces of old friends: emerging new roles of RNA-binding proteins in the DNA double-strand break response. Front. Mol. Biosci. *8*, 668821. https://doi.org/10.3389/fmolb.2021.668821.
12. Domingo-Prim, J., Bonath, F., and Visa, N. (2020). RNA at DNA double-strand breaks: the challenge of dealing with DNA:RNA hybrids. Bioessays *42*, e1900225. https://doi.org/10.1002/bies.201900225.
13. Sharma, S., Anand, R., Zhang, X., Francia, S., Michelini, F., Galbiati, A., Williams, H., Ronato, D.A., Masson, J.Y., Rothenberg, E., et al. (2021). MRE11-RAD50-NBS1 complex is sufficient to promote transcription by RNA polymerase II at double-strand breaks by melting DNA ends. Cell Rep. *34*, 108565. https://doi.org/10.1016/j.celrep.2020.108565.
14. Francia, S., Michelini, F., Saxena, A., Tang, D., de Hoon, M., Anelli, V., Mione, M., Carninci, P., and d'Adda di Fagagna, F. (2012). Site-specific DICER and DROSHA RNA products control the DNA-damage response. Nature *488*, 231–235. https://doi.org/10.1038/nature11179.
15. Michelini, F., Pitchiaya, S., Vitelli, V., Sharma, S., Gioia, U., Pessina, F., Cabrini, M., Wang, Y., Capozzo, I., Iannelli, F., et al. (2017). Damage-induced lncRNAs control the DNA damage response through interaction with DDRNAs at individual double-strand breaks. Nat. Cell Biol. *19*, 1400–1411. https://doi.org/10.1038/ncb3643.
16. Jaafar, L., Li, Z., Li, S., and Dynan, W.S. (2017). SFPQ*NONO and XLF function separately and together to promote DNA double-strand break repair via canonical nonhomologous end joining. Nucleic Acids Res. *45*, 1848–1859. https://doi.org/10.1093/nar/gkw1209.
17. Wang, Y.L., Zhao, W.W., Shi, J., Wan, X.B., Zheng, J., and Fan, X.J. (2023). Liquid-liquid phase separation in DNA double-strand breaks repair. Cell Death Dis. *14*, 746. https://doi.org/10.1038/s41419-023-06267-0.
18. Levone, B.R., Lenzken, S.C., Antonaci, M., Maiser, A., Rapp, A., Conte, F., Reber, S., Mechtersheimer, J., Ronchi, A.E., Mühlemann, O., et al. (2021). FUS-dependent liquid-liquid phase separation is important for DNA repair initiation. J. Cell Biol. *220*, e202008030. https://doi.org/10.1083/jcb.202008030.
19. Chuang, T.W., Lu, C.C., Su, C.H., Wu, P.Y., Easwvaran, S., Lee, C.C., Kuo, H.C., Hung, K.Y., Lee, K.M., Tsai, C.Y., and Tarn, W.Y. (2019). The RNA processing factor Y14 participates in DNA damage response and repair. iScience *13*, 402–415. https://doi.org/10.1016/j.isci.2019.03.005.
20. Chuang, T.W., Su, C.H., Wu, P.Y., Chang, Y.M., and Tarn, W.Y. (2023). LncRNA HOTAIRM1 functions in DNA double-strand break repair via its association with DNA repair and mRNA surveillance factors. Nucleic Acids Res. *51*, 3166–3184. https://doi.org/10.1093/nar/gkad143.
21. Yu, C.L., Chuang, T.W., Samuel, S.Y., Lou, Y.C., and Tarn, W.Y. (2023). Co-phase separation of Y14 and RNA in vitro and its implication for DNA repair. RNA *29*, 1007–1019. https://doi.org/10.1261/rna.
22. Hsu, I.W., Hsu, M., Li, C., Chuang, T.W., Lin, R.I., and Tarn, W.Y. (2005). Phosphorylation of Y14 modulates its interaction with proteins involved in mRNA metabolism and influences its methylation. J. Biol. Chem. *280*, 34507–34512. https://doi.org/10.1074/jbc.M507658200.
23. Dall'Agnese, G., Dall'Agnese, A., Banani, S.F., Codrich, M., Malfatti, M.C., Antoniali, G., and Tell, G. (2023). Role of condensates in modulating DNA repair pathways and its implication for chemoresistance. J. Biol. Chem. *299*, 104800. https://doi.org/10.1016/j.jbc.2023.104800.
24. Kilic, S., Lezaja, A., Gatti, M., Bianco, E., Michelena, J., Imhof, R., and Altmeyer, M. (2019). Phase separation of 53BP1 determines liquid-like behavior of DNA repair compartments. EMBO J. *38*, e101379. https://doi.org/10.15252/embj.2018101379.
25. Kroschwald, S., Maharana, S., and Simon, A. (2017). Hexanediol: a chemical probe to investigate the material properties of membrane-less compartments. Matters, 1–7. https://doi.org/10.19185/matters.201702000010.
26. Tacke, R., and Manley, J.L. (1999). Determinants of SR protein specificity. Curr. Opin. Cell Biol. *11*, 358–362.

27. Zahler, A.M., Lane, W.S., Stolk, J.A., and Roth, M.B. (1992). SR proteins: a conserved family of pre-mRNA splicing factors. Genes Dev. *6*, 837–847.

28. Banani, S.F., Lee, H.O., Hyman, A.A., and Rosen, M.K. (2017). Biomolecular condensates: organizers of cellular biochemistry. Nat. Rev. Mol. Cell Biol. *18*, 285–298. https://doi.org/10.1038/nrm.2017.7.

29. Mao, A.H., Crick, S.L., Vitalis, A., Chicoine, C.L., and Pappu, R.V. (2010). Net charge per residue modulates conformational ensembles of intrinsically disordered proteins. Proc. Natl. Acad. Sci. USA *107*, 8183–8188. https://doi.org/10.1073/pnas.0911107107.

30. Dawicki-McKenna, J.M., Langelier, M.F., DeNizio, J.E., Riccio, A.A., Cao, C.D., Karch, K.R., McCauley, M., Steffen, J.D., Black, B.E., and Pascal, J. M. (2015). PARP-1 Activation Requires Local Unfolding of an Autoinhibitory Domain. Mol. Cell *60*, 755–768. https://doi.org/10.1016/j.molcel.2015.10.013.

31. Heyza, J.R., Mikhova, M., Bahl, A., Broadbent, D.G., and Schmidt, J.C. (2023). Systematic analysis of the molecular and biophysical properties of key DNA damage response factors. eLife *12*, e87086. https://doi.org/10.7554/eLife.87086.

32. Mikhova, M., Goff, N.J., Janovič, T., Heyza, J.R., Meek, K., and Schmidt, J. C. (2024). Single-molecule imaging reveals the kinetics of non-homologous end-joining in living cells. Nat. Commun. *15*, 10159. https://doi.org/10.1038/s41467-024-54545-y.

33. Singatulina, A.S., Hamon, L., Sukhanova, M.V., Desforges, B., Joshi, V., Bouhss, A., Lavrik, O.I., and Pastré, D. (2019). PARP-1 activation directs FUS to DNA damage sites to form PARG-reversible compartments enriched in damaged DNA. Cell Rep. *27*, 1809–1821.e5. https://doi.org/10.1016/j.celrep.2019.04.031.

34. Zhou, Y., Lee, J.H., Jiang, W., Crowe, J.L., Zha, S., and Paull, T.T. (2017). Regulation of the DNA damage response by DNA-PKcs inhibitory phosphorylation of ATM. Mol. Cell *65*, 91–104. https://doi.org/10.1016/j.molcel.2016.11.004.

35. Romani, A., and Scarpa, A. (1992). Regulation of cell magnesium. Arch. Biochem. Biophys. *298*, 1–12.

36. Maeshima, K., Matsuda, T., Shindo, Y., Imamura, H., Tamura, S., Imai, R., Kawakami, S., Nagashima, R., Soga, T., Noji, H., et al. (2018). A transient rise in free Mg(2+) ions released from ATP-Mg hydrolysis contributes to mitotic chromosome condensation. Curr. Biol. *28*, 444–451.e6. https://doi.org/10.1016/j.cub.2017.12.035.

37. Gibson, B.A., Doolittle, L.K., Schneider, M.W.G., Jensen, L.E., Gamarra, N., Henry, L., Gerlich, D.W., Redding, S., and Rosen, M.K. (2019). Organization of chromatin by intrinsic and regulated phase separation. Cell *179*, 470–484.e21. https://doi.org/10.1016/j.cell.2019.08.037.

38. Sigala, I., Koutroumani, M., Koukiali, A., Giannakouros, T., and Nikolakaki, E. (2021). Nuclear translocation of SRPKs is associated with 5-FU and cisplatin sensitivity in HeLa and T24 cells. Cells *10*, 759. https://doi.org/10.3390/cells10040759.

39. Li, L., Yao, L., Wang, M., Zhou, X., and Xu, Y. (2024). Phase separation in DNA damage response: New insights into cancer development and therapy. Biochim. Biophys. Acta. Rev. Cancer *1879*, 189206. https://doi.org/10.1016/j.bbcan.2024.189206.

40. Lou, Y.C., Tu, C.F., Chou, C.C., Yeh, H.H., Chien, C.Y., Sadotra, S., Chen, C., Yang, R.B., and Hsu, C.H. (2024). Structural insights into the role of N-terminal integrity in PhoSL for core-fucosylated N-glycan recognition. Int. J. Biol. Macromol. *255*, 128309. https://doi.org/10.1016/j.ijbiomac.2023.128309.

41. Nagy, Z., Comer, S., and Smolenski, A. (2018). Analysis of Protein Phosphorylation Using Phos-Tag Gels. Curr. Protoc. Protein Sci. *93*, e64. https://doi.org/10.1002/cpps.64.

STAR★METHODS

KEY RESOURCES TABLE

REAGENT or RESOURCE	SOURCE	IDENTIFIER
Antibodies		
Mouse monoclonal anti-phospho-Histone H2A.X (Ser139) (γH2AX)	Millipore	Cat# 05–636; RRID: AB_309864
Mouse monoclonal anti-DNA PKcs	Abcam	Cat# ab44815; RRID: AB_731982
Mouse monoclonal anti-FUS/TLS	Santa Cruz Biotechnology	Cat# sc-47711; RRID: AB_2105208
Mouse monoclonal anti-Poly(ADP-ribose) (PAR)	Enzo Life Sciences	Cat# BML-SA216-0100; RRID: AB_2052274
Mouse monoclonal anti-GAPDH	Proteintech	Cat# 60004-1-Ig; RRID: AB_2107436
Mouse monoclonal anti-SRPK1	BD Biosciences	Cat# 611072; RRID: AB_398385
Rabbit monoclonal anti-Ku70	Cell Signaling Technology	Cat# 4588; RRID: AB_11179211
Rabbit polyclonal anti-RBM8A (Y14)	GeneTex	Cat# 131387; RRID: AB_2886473
Rabbit polyclonal anti-Histone H2AX [p Ser139] (γH2AX)	Novus Biologicals	Cat# NB100-384; RRID: AB_10002815
Rabbit polyclonal anti-NHEJ1 (XLF)	ABclonal	Cat# 19957
Rabbit polyclonal anti-LIG4 (DNA ligase 4)	Proteintech	Cat# 12695-1-AP; RRID: AB_2136253
Rabbit polyclonal anti-GST	Sigma-Aldrich	Cat# 06–332; RRID: AB_310104
Rabbit polyclonal anti-FLAG tag	Sigma-Aldrich	Cat# SAB4301135; RRID: AB_2811010
Goat anti-mouse IgG, Alexa Fluor^{TM} 488	Thermo Fisher Scientific	Cat# A11001; RRID: AB_2534069
Goat anti-mouse IgG, Alexa Fluor^{TM} 568	Thermo Fisher Scientific	Cat# A11001; RRID: AB_144696
Goat anti-rabbit IgG, Alexa Fluor^{TM} 568	Thermo Fisher Scientific	Cat# A11011; RRID: AB_143157
FITC-conjugated goat anti-Rabbit IgG	MP BIomedicals	Cat# 55646
Chemicals, peptides, and recombinant proteins		
Chemicals		
SRPIN340 (SRPK1 inhibitor)	MedChemExpress	Cat# HY-13949
KU55933 (ATM inhibitor)	Tocris Bioscience	Cat# 3544
VE-821 (ATR inhibitor)	Sigma-Aldrich	Cat# SML1415
NU7441 (DNA-PK inhibitor)	Tocris Bioscience	Cat# 3712
Mirin (MRE11 inhibitor)	Sigma-Aldrich	Cat# M9948
Olaparib	LC Laboratories	Cat# O-9201
1, 6-hexanediol	Sigma-Aldrich	Cat# 240117
5,6-dichloro-1-β-D-ribofuranosylbenzimidazole (DRB)	Sigma-Aldrich	Cat# D1916
EDTA-AM (EDTA acetoxymethyl ester)	MedChemExpress	Cat# HY-D1746
HaloTag® TMR Ligand	Promega	Cat# G825A
HaloTag® TMRDirect^{TM} Ligand	Promega	Cat# G299A
Phos-tag^{TM} Acrylamide AAL-107	NARD Institute	Cat# 304-93521
Alexa Fluor^{TM} 488 C_5 Maleimide	Thermo Fisher Scientific	Cat# A10254
FlexAble CoraLite® Plus 647 antibody labeling kit for rabbit IgG	Proteintech	Cat# KFA003
Cyanine 5-UTP	Enzo Life Sciences	Cat# ENZ-42506
Biotin (Terminal) PAR	R&D Systems	Cat# 4336-100-02
(S)-(+)-Camptothecin (CPT)	Sigma-Aldrich	Cat# C9911
Dulbecco's modified Eagle's medium (DMEM)	Gibco	Cat# 11965-092
McCoy's 5A medium	Gibco	Cat# 16600-082
Fetal Bovine Serum (FBS)	Corning	Cat# 35-010-CV

(*Continued on next page*)

Continued

REAGENT or RESOURCE	SOURCE	IDENTIFIER
L-glutamine	Gibco	Cat# A29168-01
penicillin and streptomycin	Gibco	Cat# 15140-122
Lipofectamine^{TM} 2000 Transfection Reagent	Thermo Fisher Scientific	Cat# 11668500
Dynabeads MyOne Streptavidin C1	Thermo Fisher Scientific	Cat# 65001
T7 RNA polymerase	Promega	Cat# P2075
Artemis peptide	Kelowna International Scientific Inc.	N/A
Ku70-1 peptide	Kelowna International Scientific Inc.	N/A
Ku70-2 peptide	Kelowna International Scientific Inc.	N/A
recombinant GST protein	Chuang et al.[19]	N/A
recombinant GST-Y14 protein	Chuang et al.[19]	N/A
recombinant GST-Y14ΔC protein	Chuang et al.[19]	N/A
recombinant Y14 protein	This study	N/A
recombinant Y14SD protein	This study	N/A
recombinant human XRCC5 and XRCC6 (Ku70/80) heterodimer protein	Sino Biological	Cat# CT018-H07B
recombinant SRPK protein	MyBioSource	Cat# MBS2545534
Critical commercial assays		
Cell Counting Kit-8	Enzo Life Sciences	Cat# ALX-850-039
Genious 2X SYBR Green Fast qPCR mix	ABclonal	Cat# RK21204
Experimental models: Cell lines		
U2OS	Lab stock	N/A
HeLa	Lab stock	N/A
Oligonucleotides		
All oligonucleotides used in this were listed in Table S1	This study	N/A
Recombinant DNA		
pcDNA3.1-Halo-Y14	This study	N/A
pcDNA3.1-Halo-Y14SA	This study	N/A
pcDNA3.1-Halo-Y14WV	This study	N/A
pcDNA3.1-Halo-Y14ΔC	This study	N/A
pcDNA3.1-Halo-Y14 siRNA resistant	This study	N/A
pET-His-GB1-Y14	This study	N/A
pET-His-GB1-Y14SD	This study	N/A
Software and algorithms		
ZEN (Black Edition)	ZEISS	https://www.micro-shop.zeiss.com/en/us/softwarefinder/software-categories/zen-black/; RRID:SCR_018163
GraphPad Prism (version 9)	GraphPad Software	https://www.micro-shop.zeiss.com/en/us/softwarefinder/software-categories/zen-black/; RRID:SCR_018163
ImageJ	National Institutes of Health	https://imagej.net/ij/; RRID:SCR_003070
Other		
HiPrep Heparin FF 16/10 column	Sigma-Aldrich	Cat# GE28-9365-49
Amicon Ultra-15 device	Millipore	Cat# UFC910096
Mendeley Data	This study	https://doi.org/10.17632/vfj43k8h29.1

EXPERIMENTAL MODEL AND STUDY PARTICIPANT DETAILS

Cell lines and cell cultures

U2OS cell line was cultured in McCoy's 5A medium (Gibco). HeLa cell line was cultured in DMEM (Gibco). All media were supplemented with 10% FBS (Corning), 100 U/mL penicillin and streptomycin (Gibco) and 2 mM L-glutamine (Gibco). All cell lines were incubated at 37°C and with 5% CO$_2$.

METHOD DETAILS

Plasmid construction

The expression vectors encoding FLAG-Y14, FLAG-Y14SA and GST-Y14 were described previously.[19] The HaloTag and human Y14 cDNAs were in frame ligated into pCDNA3.1 (Thermo Fisher Scientific) to create the Halo-Y14 expression vector. The SA, WV, ΔC and siRNA resistant mutants of Halo-Y14 were generated by PCR-based mutagenesis or deletion; the sequence of all plasmids was verified by Sanger sequencing. For recombinant Y14 protein (see below), we constructed a His-GB1-Y14 expression vector by cloning the Y14 coding region into the pET-GB1 expression vector.[40] The SD mutant was generated using PCR-based methods.

Cell culture, transfection, and drug treatment

U2OS cells and HeLa cells were cultured in 10% fetal bovine serum-containing McCoy's 5A and DMEM medium (Gibco) respectively. For transient transfection, Lipofectamin 2000 (Thermo Fisher Scientific) was used according to manufacturer's instruction as described previously.[20] Gapmers used for depleting *HOTAIRM1* were as described.[20] Cells were collected 48 hrs post-transfection for subsequent imaging of Halo-Y14 or RT-PCR (primers as listed in Table S1). Ionizing radiation was performed using RS 2000 X-ray Biological Irradiator (Rad Source). Pharmacological treatment was carried out as following: 50 μM SRPK1 inhibitor SRPIN340 (MedChemExpress) for 48 hrs, 10 μM ATM inhibitor KU55933 (Tocris) for 1 hour, 10 μM ATR inhibitor VE-821 (Sigma-Aldrich) for 1 hr, 10 μM DNA-PK inhibitor NU7441 (Tocris) for 1 hr, 500 μM MRE11 inhibitor Mirin (Sigma-Aldrich) for 2 hr, 1 μM Olaparib (LC Laboratories) for 1 hr, 4% 1,6-hexanediol (Sigma-Aldrich) for 30 min, 100 μM 5,6-dichloro-1-β-D-ribofuranosylbenzimidazole (DRB, Sigma-Aldrich) for 3 h or 20 μM EDTA-AM (MedChemExpress) for 2 hrs.

Laser microirradiation and fluorescence imaging

Laser microirradiation using a laser-scanning confocal microscope (LSM 880, Carl Zeiss) with 405 nm laser diode was as described.[20] For live cell imaging, U2OS cells were transiently transfected with the Halo-Y14 vector. After 48 hours, cells were incubated with 5 μM HaloTag tetramethylrhodamine (TMR) ligand (Promega) for 1 hour before laser microirradiation using laser diodes at 405 nm and visualized at 561 nm in a LSM 880 confocal microscope (Carl Zeiss). For cell fixation, 4% paraformaldehyde and 0.5% Triton X-100 in PBS were used. Following, cells were incubated with 5 μM HaloTag TMRDirect Ligand (Promega) overnight at 4°C. Immunofluorescence was performed as described.[20] Primary antibodies used included polyclonal RBM8A/Y14 (GeneTex), γH2AX (Novus), Ku70 (Cell Signaling), NHEJ1 (XLF) (ABclonal) and LIG4 (DNA ligase 4) (Proteintech), and monoclonal γH2AX (Millipore), DNA-PKcs (Abcam), FUS (Santa Cruz), PAR (Enzo Life Sciences) and SRPK1 (BD Biosciences). Secondary antibodies included Alexa fluor 488-conjugated anti-mouse IgG, Alexa fluor 568-conjugated anti-mouse IgG, Alexa fluor 568-conjugated anti-rabbit IgG (all of above from Thermo Fisher Scientific), FITC-conjugated anti-rabbit IgG (Cappel), or FlxAble CoraLite Plus 647 (Proteintech)-conjugated anti-rabbit IgG. Nuclei were counterstained in Mounting Medium with 4',6-diamidino-2-phenylindole (DAPI; Sigma-Aldrich). Samples were visualized using a confocal laser scanning microscope (LSM 880, Carl Zeiss) coupled with an image analysis system. To quantify PAR signals, the same region of interest (ROI) between control and experiment groups was compared. The recruitment fold for Halo-Y14, NHEJ factors and FUS was calculated by (ROI of LMI region – ROI of non-LMI region)/ROI of non-LMI region.

Immunoblotting

Immunoblotting was performed as described.[22] Primary antibodies used included polyclonal RBM8A/Y14 (GeneTex) and monoclonal GAPDH (ProteinTech) and GST (Sigma-Aldrich).

Purification of recombinant non-tagged Y14 protein

The pET-GB1-Y14 plasmid was transformed into *E. coli* strain BL21 (DE3). Bacteria were grown at 37°C till OD$_{600}$ reached 0.6. Recombinant protein expression was induced by 1 mM isopropyl β-D-1-thiogalactopyranoside (IPTG) at 25°C overnight. Bacteria were collected and cell pellet was resuspended in a buffer containing 50 mM Tris-HCl (pH 8.0), 750 mM NaCl, and 5% glycerol, and lysed using an N-2 NanoLyzer-N2 (Gogene Corporation). The lysate was centrifuged at 12,000×g for 30 minutes at 4°C. The supernatant was applied to a Ni-NTA resin column (GE Healthcare) and eluted with the above buffer containing 200 mM imidazole. The eluate was then dialyzed against a buffer containing 20 mM phosphate (pH 7), 50 mM KCl, and subsequently loaded onto a HiPrep Heparin FF 16/10 column (GE Healthcare). The column was washed with a buffer containing 20 mM phosphate (pH 7) and 20 mM KCl. Elution was performed using a linear KCl gradient from 20 mM to 1 M in buffer. GB1-Y14 was eluted at approximately 0.55 M KCl. The eluate was dialyzed against a buffer containing 50 mM HEPES (pH 8), 100 mM KCl, and 1 mM DTT, and then treated with TEV protease overnight at 4°C. Ni-NTA affinity chromatography was used to remove the fusion tags. The flow-through was buffer-exchanged to a storage buffer containing 50 mM HEPES (pH 8) and 300 mM KCl. Purified recombinant Y14 was concentrated using an Amicon Ultra-15 device (Merck Millipore) and stored at -80°C. Recombinant Y14SD and Y14ΔC were purified similarly to wild-type Y14. Protein concentration was measured by absorbance at 280 nm, using extinction coefficients (ε) calculated with the ProtParam tool. In all experiments, the A260/280 absorbance ratios of purified proteins ranged from 0.5 to 0.6.

In vitro phosphorylation of recombinant Y14

Purified recombinant Y14 was *in vitro* phosphorylated by SRPK1 (MyBioSource) at a molar ratio of 400:1 in a buffer containing 20 mM HEPES (pH7.9), 50 mM KCl, 2 mM $MgCl_2$, and 2 mM ATP at 30°C for 4-5 hrs. Buffer exchange was performed using PD SpinTrap^{TM} G-25 (Cytiva). Phosphorylated Y14 (pY14) was stored in a buffer containing 50 mM HEPES and 300 mM KCl (pH 8).

Phos-tag gel electrophoresis

Phos-tag^{TM} SDS-polyacrylamide gel electrophoresis (PAGE) was performed on a 12% SDS-polyacrylamide gel containing 50 µM Phos-tag acrylamide AAL-107 (NARD Institute) and 100 µM $MnCl_2$ according to the manufacturer's instruction (FUJIFILM Wako). pY14 was denatured in Laemmli SDS Sample Buffer (65 mM Tris, pH6.8, 2% SDS, 10% glycerol, 5% 2-mercaptoethanol, 0.005% bromophenol blue) at 95°C for 5 min before electrophoresis. ToolStart Blue Staining Reagent (BIOTOOLS) was used for gel staining. To analyze endogenous Y14 on Phos-tag gels, U2OS cells were treated with SRPI340 as described above, and cell lysates were prepared using RIPA buffer containing 50 mM Tris-HCl (pH 7.4), 150 mM NaCl, 1 mM EDTA, 1% NP-40, 1% sodium deoxycholate, and 0.1% SDS. As a control, cell lysate was treated with alkaline phosphatase (FastAP, Thermo Fisher Scientific) for 1 hour. Phos-tag SDS-PAGE was modified according to Nagy et al.[41] To prevent EDTA chelation, 1 mM $ZnCl_2$ was added to the lysates. Electrophoresis was performed on a gel containing 10% bis-acrylamide (29:1), 350 mM Bis-Tris-HCl (pH 6.8), 35 µM Phos-tag, and 70 µM $ZnCl_2$ using buffer containing 0.1 M Tris-base, 0.1 M MOPS (pH7.8) with 0.1% SDS and 5 mM $NaHSO_3$. The gel was washed with the transfer buffer containing 25 mM Tris-base, 192 mM glycine, 10 mM EDTA and 10% methanol three times, followed by EDTA-free transfer buffer twice (20 min for each wash). Immunoblotting was as described.[22]

Fluorescent labeling of proteins

For fluorescent labeling, recombinant pY14 or Ku70/80 heterodimer (Sino Biological) was incubated with Alexa Fluor^{TM} 488 C_5 Maleimide (Thermo Fisher Scientific) in a 1:20 molar ratio of protein to dye at 4°C overnight. Unlabeled dye was removed by using microspin column PD SpinTrap^{TM} G-25 (Cytiva).

In vitro transcription and Cy5-labeling of RNA

The vector for expressing full-length *HOTAIRM1* (1044 nucleotides in length) was described previously.[21] *In vitro* transcription of *HOTAIRM1* was carried by using linearized plasmid as template in the presence of T7 RNA Polymerase (Promega) and 2 mM NTPs at 37°C for 1 hr. To Cy5-label RNA, 2 mM ATP, CTP and GTP, 1.8 mM UTP and 0.2 mM of Cy5-UTP (Enzo Life Science) were used. RNA was purified by phenol-chloroform extraction.

Liquid-liquid phase separation (LLPS) assay

For LLPS of Y14, 20 µM recombinant Y14 was incubated in a buffer containing 20 mM HEPES (pH 7.2) and 50 mM KCl at room temperature for 20 minutes. For LLPS of pY14, 2.5 mM $MgCl_2$ and 3% polyethylene glycol (PEG) 6000 were added. For heterotypic LLPS, 0.5 µM Alexa 488-labeled Ku70/80 and/or 0.2 µM Cy5-labeled *HOTAIRM1* RNA were added into pre-formed pY14 droplets. Droplets were visualized on cover glasses for 10 minutes using Leica DMI6000B with a 100× oil immersion objective. To determine the partition coefficient (K), 2 µM TAMRA-labeled IDR peptide was added into pre-formed pY14 droplets and incubated in confocal dishes at room temperature for 30 min. Fluorescence images were acquired using a Zeiss LSM 780 confocal microscope with a 561 nm excitation laser. Six different fields of view containing 70-250 droplets were used. Fluorescence intensities of the droplets were measured by averaging the intensities at their centers. K was calculated as $I_{droplet} / I_{bulk}$ ($I_{droplet}$ and I_{bulk} represented the intensity of droplets and bulk regions, respectively). Statistical significance was assessed using an unpaired t-test.

Fluorescence recovery after photo bleaching (FRAP)

FRAP experiments were performed using an inverted confocal microscope (LSM 780, Carl Zeiss) equipped with a Plan-Apochromat 100×1.4 Oil DIC M27 oil-immersion objective. Alexa 488-labeled Y14/pY14 (0.5 µM) were mixed with unlabeled Y14/pY14 (20 µM) in the above Mg^{2+}/PEG-containing LLPS buffer in a confocal dish (SPL Life Sciences) for 30 minutes. Droplets with sizes ranging from 7 to 30 μm^2 were selected. Bleaching was conducted with a 488 nm laser operating at 100% laser power. The bleached region of interest (ROI) was fixed at 1.22 μm^2 (< 20% of the total droplet area). Time-lapse images were captured at 10-second intervals over a total duration of 200 seconds. At least 5 droplets from three independent experiments were collected for analysis. FRAP data were analyzed using ZEN (Black Edition) software to quantify fluorescence intensity changes over time. The normalized fluorescence intensity $I_{norm}(t)$ was calculated as following: $\frac{I_{bleach}(t) - I_b}{I_{non-bleach}(t) - I_b}$ (I_{bleach}, $I_{non-bleach}$, and I_b represented the intensity of bleached ROI, non-bleached ROI, and background, respectively).

Turbidity measurements

Turbidity was measured by monitoring the optical density (OD) at 340 nm using a NanoDrop ND-1000 spectrophotometer (Thermo Fisher Scientific).

Far-western blot analysis

For far-western blot analysis, 2 μg of recombinant pY14 was resolved on a 12% native polyacrylamide gel using a running buffer containing 25 mM Tris-HCl and 100 mM glycine (pH 8.9), and transferred onto a nitrocellulose membrane (Amersham^{TM}, GE Healthcare). After staining with Ponceau S, a section of the membrane containing pY14 was excised and blocked with 5% BSA-containing TBST (100 mM Tris-base, pH 7.6, 154 mM NaCl, 0.1% Tween-20) for 30 minutes at room temperature. After washing, the membrane was incubated with 30 or 60 ng of TAMRA-labeled IDR peptides in 1 ml of the buffer containing 20 mM HEPES, 50 mM KCl, pH7.2 at room temperature for 30 min. The membrane was washed three times with TBS (100 mM Tris-HCl, pH 7.6, and 154 mM NaCl). Fluorescent signals were detected using the Alexa Fluor 555 channel on an iBright^{TM} FL1500 Imaging System. Quantification was performed using ImageJ by selecting equally sized regions of interest (ROIs) across membranes.

Nonhomologous end joining (NHEJ) assay

The Cas9/sgRNA-based NHEJ assay was previously described.[20] In principle, the Cas9/ sgHPRT-expressing vector (Table S1) and double-stranded DNA oligonucleotides Ins (Table S1, Thermo Fisher Scientific) were transfected into U2OS cells. To analyze the effect of Y14, Y14-targeting siRNA (siY14) and siRNA-resistant Halo-Y14 vector were cotransfected. Genomic DNA was collected 48 hrs post-transfection and analyzed by quantitative PCR (qPCR) using primers as listed in Table S1.

RT-PCR and qPCR

For RT-PCR, total cellular RNA was extracted using TRIzol reagent (Thermo Fisher Scientific) and treated with RNase-free DNase I (Promega). For reverse transcription, Random Hexamer Primer and Superscript III Reverse Transcriptase (both from Thermo Fisher Scientific) were used. Real-time qPCR was conducted in a 20-μl reaction, containing 100 ng genomic DNA or cDNAs, 500 nM primers and 10 μl of a SYBR Green Fast qPCR Mix (ABclonal) on a LightCycler 480 Real-Time PCR System (Roche). Gene-specific primers were listed in Table S1. The Student's t-test was used to analyze differential expression in triplicate.

PAR binding assay

Recombinant GST and GST-Y14 proteins were prepared as described.[22] Biotin-labeled poly ADP-ribose (PAR) polymer (R&D Systems) was incubated with GST and GST-Y14 at a final concentration of 1 μM for 2 hrs at room temperature in NETN buffer containing 0.5% NP-40, 0.5 mM EDTA, 50 mM Tris-HCl pH 8.0, 100 mM NaCl with protease inhibitors (Roche) and was then pulled down by magnetic streptavidin beads (Thermo Fisher Scientific).

Cell proliferation assay

Cell proliferation was assessed using the Cell Counting Kit-8 (CCK-8) assay (Enzo Life Sciences). U2OS or HeLa cells were seeded at a density of 2×10^4 cells per well in 96-well plates for overnight, followed by SRPIN340 treatment for 24 hrs. Cells were subjected to different doses of IR before the CCK-8 assay. For camptothecin (CPT) treatment, an 8-hr treatment with SRPIN340 was followed by 16 hours of incubation with CPT. The CCK-8 assay was performed according to manufacturer's instruction. Absorbance at 450 nm was measured using a microplate reader.

Colony formation assay

U2OS or HeLa cells were seeded at a density of 400 cells per well in 6-well plates and treated as in the cell proliferation assay. Cells were seeded for an additional 10 days to allow colony formation. To count colonies, cells were fixed with 4% paraformaldehyde and stained with 0.01% crystal violet. Colonies containing at least 50 cells were counted. The survival fraction was calculated by comparing the number of cells in the treatment and control groups.

QUANTIFICATION AND STATISTICAL ANALYSIS

Statistical analyses were essentially performed by a two-tailed, unpaired Student's t-test using Prism (GraphPad) in this study. Data were presented as mean ± SD. In all statistic analysis, P-values are denoted by asterisks: * $p<0.05$; ** $p<0.01$; *** $p<0.001$; **** $p<0.0001$; ns: no statistical significance. P-values and *N* numbers are indicated in the figures or in the figure legends.